Materials Research Letters

ISSN: 2166-3831 (Online) Journal homepage: www.tandfonline.com/journals/tmrl20

Exceptional magnetic shielding via ultra-low-remanence co-based amorphous alloys engineered by atomic ordering

Yuyang Qian , Chaoqun Pei , Congrui Yang , Zida Zhang , Zhichao Lu , Dong Ma , Ke Yang , Jiang Ma , Baoan Sun , Haibo Ke , Gang Wang & Weihua Wang

To cite this article: Yuyang Qian , Chaoqun Pei , Congrui Yang , Zida Zhang , Zhichao Lu , Dong Ma , Ke Yang , Jiang Ma , Baoan Sun , Haibo Ke , Gang Wang & Weihua Wang (20 Apr 2026): Exceptional magnetic shielding via ultra-low-remanence co-based amorphous alloys engineered by atomic ordering, Materials Research Letters, DOI: 10.1080/21663831.2026.2660809

To link to this article: https://doi.org/10.1080/21663831.2026.2660809

MATER. RES. LETT.
https://doi.org/10.1080/21663831.2026.2660809

MATERIALS RESEARCH LETTERS
Taylor & Francis by informa

ORIGINAL REPORT

OPEN ACCESS Check for updates

Exceptional magnetic shielding via ultra-low-remanence co-based amorphous alloys engineered by atomic ordering

Yuyang Qian[a,b*], Chaoqun Pei[a,c*], Congrui Yang[a], Zida Zhang[a,d], Zhichao Lu[a], Dong Ma[a], Ke Yang[e], Jiang Ma[c], Baoan Sun[a,d], Haibo Ke[a,f], Gang Wang[b] and Weihua Wang[a,f,d]

[a]Songshan Lake Materials Laboratory, Dongguan, Guangdong 523808, People's Republic of China; [b]Dongguan Institute of Materials Science and Technology, Chinese Academy of Sciences, Dongguan, Guangdong 523808, People's Republic of China; [c]Shenzhen Key Laboratory of High Performance Nontraditional Manufacturing, College of Mechatronics and Control Engineering, Shenzhen University, Shenzhen 518060, People's Republic of China; [d]Institute of Physics, Chinese Academy of Sciences, Beijing 100190, People's Republic of China; [e]State key laboratory of Materials for Advanced Nuclear Energy, Shanghai University, Shanghai 200444, People's Republic of China; [f]Shanghai Synchrotron Radiation Facility, Shanghai Advanced Research Institute, Chinese Academy of Sciences, Shanghai, 201204, People's Republic of China

ABSTRACT

Ubiquitous electromagnetic signals enable modern information exchange but also cause radiation, interference, and data security risks. Shielding low-frequency magnetic fields (f $<$ 100 kHz) remains challenging because conventional materials exhibit high residual magnetization that weakens shielding performance. Here, ultra-low residual magnetization in Co-based amorphous alloys is achieved through atomic ordering induced by multi-step rotating magnetic field (MS-RMF) annealing. The alloys show ultra-low coercivity (0.147 A/m), residual magnetic field of $\sim$50 nT, and a maximum permeability of $\sim$400,000, resulting in a 70% improvement in magnetic shielding effectiveness by reducing magnetic anisotropy and enhancing domain wall mobility.

ARTICLE HISTORY
Received 9 March 2026

KEYWORDS
Amorphous alloy; ultra-low remanence; soft magnetic; magnetic shielding

1. Introduction

The proliferation of electronic devices and the rapid advancement of artificial intelligence have ushered in an era of ubiquitous electromagnetic signals, which form the backbone of modern information exchange. However, this electromagnetic convenience comes with significant challenges [1], including pervasive electromagnetic radiation, signal interference, and critical data security risks [2–7]. Effectively managing the electromagnetic environment has thus become a paramount concern for ensuring the reliable operation of electronic systems and protecting sensitive information [8,9]. Among the various electromagnetic threats, shielding against low-frequency magnetic fields (particularly below 100 kHz) presents a formidable technical hurdle [10,11]. These fields can easily penetrate conventional shielding barriers, causing severe malfunctions in precision electronic instruments and disrupting the detection of weak signals.

The development of current shielding materials is shifting from single-component systems towards composite and structurally-engineered designs. Examples include the stacking of multiple materials, the creation of foam-like multi-layer porous architectures [10], and the incorporation of emerging low-dimensional materials such as MXenes [12]. These approaches primarily aim to achieve lightweight and flexible characteristics. However, the shielding capability against extremely low-frequency to static magnetic fields, coupled with long-term, field-validated performance in precision scientific and industrial applications, demonstrates that traditional magnetic shielding materials remain the indispensable, foundational solution in domains where shielding effectiveness and stability are of paramount, non-negotiable importance. Traditional magnetic shielding materials [13], such as silicon steels and permalloys, are fundamental limited by high residual magnetization,

CONTACT Baoan Sun sunba@iphy.ac.cn Songshan Lake Materials Laboratory, Dongguan, Guangdong 523808, People's Republic of China; Institute of Physics, Chinese Academy of Sciences, Beijing 100190, People's Republic of China; Haibo Ke kehaibo@sslab.org.cn Songshan Lake Materials Laboratory, Dongguan, Guangdong 523808, People's Republic of China; Gang Wang g.wang@shu.edu.cn State key laboratory of Materials for Advanced Nuclear Energy, Shanghai University, Shanghai 200444, People's Republic of China

*Yuyang Qian and Chaoqun Pei contributed equally to this work.

Supplemental data for this article can be accessed online at https://doi.org/10.1080/21663831.2026.2660809.

This article has been corrected with minor changes. These changes do not impact the academic content of the article.

which leads to magnetic hysteresis that significantly degrades shielding efficiency (SE) by consuming energy and reducing magnetic permeability [14]. Furthermore, conventional annealing methods have become inadequate to meet the performance requirements demanded by advanced magnetic shielding applications. Consequently, the development of new materials with ultra-low residual magnetization and ultra-high permeability is critically needed to achieve effective low-frequency magnetic shielding.

In this work, we address this long-standing challenge through a novel material-design and processing strategy. We report on a Co-based amorphous alloy engineered to possess exceptional magnetic softness. This is achieved via a tailored multi-step rotating magnetic field (MS-RMF) annealing technique, which induces a highly ordered atomic structure. The resulting material exhibits ultra-low coercivity (0.147 A/m) and residual magnetic field ($\sim$ 50 nT) — an order of magnitude lower than those of conventional materials — coupled with an extraordinarily high maximum permeability of $\sim$ 400,000. These superior properties collectively yield a remarkable magnetic shielding effectiveness of up to 70%. Mechaistic studies confirm that the superior performance originates from the extremely low effective magnetic anisotropy and enhanced domain-wall mobility induced by the MS-RMF treatment. Our work provide a transformative pathway for designing next-generation electromagnetic shielding materials tailored for high-performance applications in sensitive low-frequency environments.

2. Results and discussion

Figure S1a presents a schematic of the multi-step vacuum rotating magnetic field (RMF) annealing system. To avoid oxidation, the chamber was first evacuated and then purged with argon before heating. The optimized annealing protocol, shown in Figure 1b, consists of three sequential steps. First, the ribbons undergo stress-relief annealing at 673 K for 60 min, followed by rapid water quenching to room temperature. Second, RMF-assisted annealing is performed at 478 K for 60 min to enhance magnetic domain alignment. Finally, the samples are quenched again to retain the microstructure established during the treatment.

As shown in Figure S1c, the ribbon-shaped samples were cut to precise dimensions and wound into toroidal cores for magnetic property characterization. Each ribbon was 5 mm wide, yielding cores with an inner diameter of 17.3 mm and an outer diameter of 19.3 mm. This geometry minimizes magnetic flux leakage during testing and ensures consistency across samples. Elemental mapping performed by energy-dispersive X-ray spectroscopy (EDX) coupled with high-resolution TEM confirms the uniform distribution of Co, Fe, Si, B, and Ni in the alloy.

Magnetic shielding materials demand not only high magnetic permeability but also extremely low residual magnetic field to prevent interference with internal components after demagnetization [11,15–20]. To meet these performance requirements, we systematically examined the influence of annealing treatments on the soft magnetic properties of the amorphous ribbons. Schematic diagrams of different annealing methods and their corresponding soft magnetic properties are shown in Figure S2.

Freshly prepared amorphous materials inherently contain residual stresses from rapid quenching or processing, these stresses are commonly relieved by structural relaxation through thermal annealing at or just below the glass transition temperature T_g, which reduces free volume and lowers residual stress levels [21–24]. Heat treatments were performed between 653 and 773 K at 20 K intervals around T_g 823 K. The resulting soft magnetic properties were evaluated, as shown in Figures 1b and c, and the XRD results are shown in Figure S3. When the temperature exceeds 773 K, the sample begins to crystallize.

The optimal magnetic performance at 673 K is likely attributable to an effective balance between stress relaxation and structural stability. At this temperature, the annealing treatment provides sufficient thermal activation to relieve the residual internal stress introduced during rapid quenching, thereby reducing local magnetoelastic anisotropy and facilitating domain-wall motion. In contrast, lower annealing temperatures may not fully relax the internal stress, while higher temperatures, particularly near 773 K, induce the onset of crystallization. The increased remanence at 773 K is likely associated with the onset of crystallization revealed by XRD. Partial crystallization can disrupt the structural homogeneity of the amorphous matrix, introduce additional magnetic anisotropy, and hinder reversible domain-wall motion, thereby deteriorating the soft-magnetic behavior and increasing the residual magnetization. This interpretation is consistent with previous reports on Co-based and other soft-magnetic amorphous alloys [25]. Therefore, 673 K is considered the optimum stress-relief condition in the present system.

Our systematic annealing experiments demonstrate that magnetic field heat treatment below the Curie temperature effectively suppresses residual magnetic field to unprecedented levels. Samples were annealed at 20 K intervals between 438 and 498 K, just below the 500 K Curie point. As shown in Figures 1e–f, both coercivity and remanence reached distinct minima at 478 K, with optimal values of 0.51 A/m and 0.0113 T, respectively.

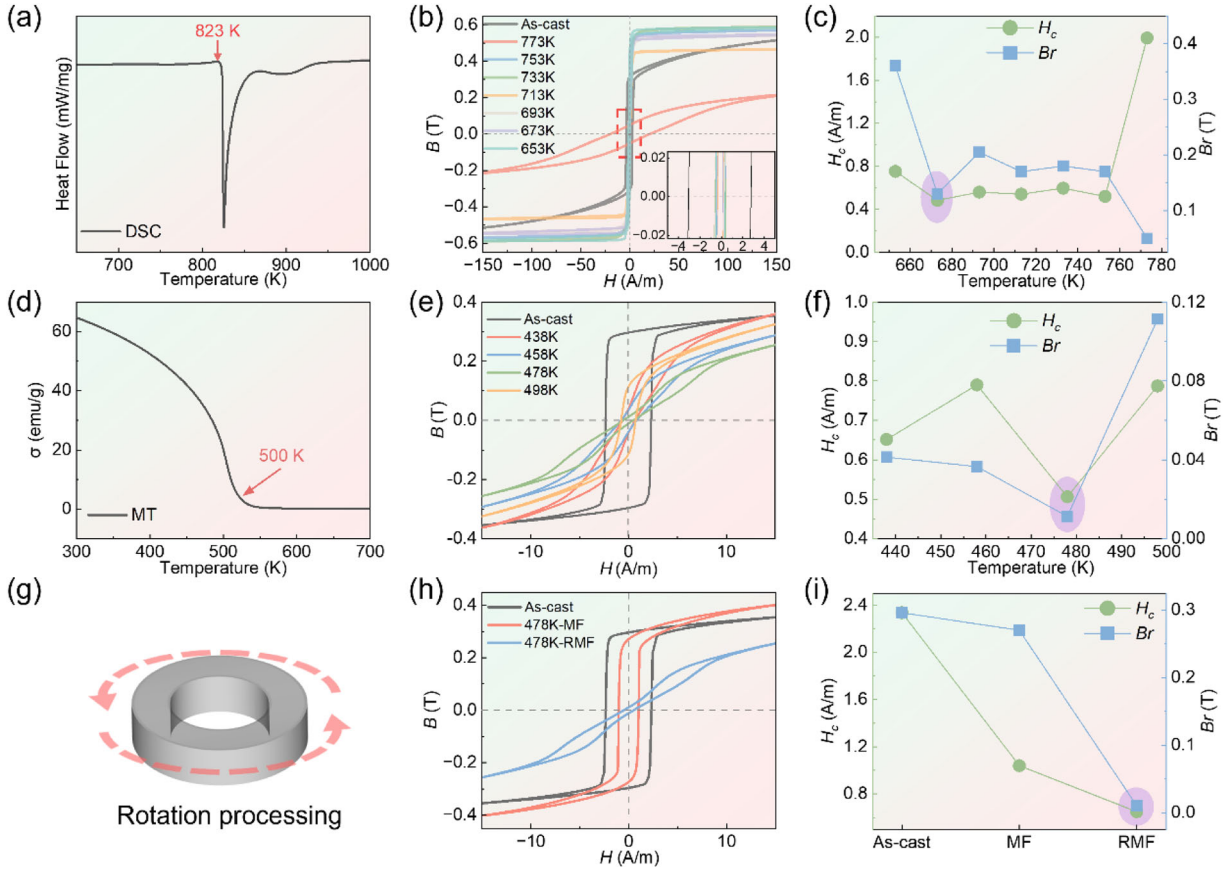

Figure 1. (a) DSC test plots of ribbon. (b) M-H curves of core around T_g. Insert (bottom right) is the amplified M-H loops. (c) Coercivity and remanence statistics around T_g. (d) Curie temperature test curve. (e) M-H curves of core around curie temperature. (f) Coercivity and remanence statistics around curie temperature. (g) Rotation processing of core. (h) M-H curves of core at different heat treatment methods. (i) Coercivity and remanence statistics at different heat treatment methods.

Moreover, the XRD results in Figure S4 demonstrate that all annealed samples are in an amorphous state. This pronounced reduction in magnetic hysteresis indicates that annealing near this critical temperature markedly enhances magnetic softness, making it a promising condition for further optimization.

Building on these results, we investigated magnetic field-assisted annealing at 478 K, comparing fixed and rotating magnetic field configurations (Figure 1g). Magnetic characterization (Figures 1(h–i)) revealed that rotating-field annealing substantially outperforms static-field annealing. Specifically, coercivity decreased from 2.33 A/m to 0.65 A/m, while remanence dropped from 0.296 to 0.01 T. This significant improvement suggests that dynamic field alignment during annealing facilitates more effective domain relaxation [26,27], providing a promising strategy for optimizing soft magnetic performance.

Based on our experimental findings, stress-relief annealing at 673 K significantly reduced sample coercivity, while rotating magnetic field-assisted annealing below the Curie temperature effectively suppressed remanence. A logical next step was to investigate whether combining these treatments could synergistically achieve both low coercivity and low remanence. To this end, we designed a two-step annealing process that integrates both strategies. The results presented in Figure 2a confirm that this combined approach yields samples with optimized soft magnetic properties, which is further supported by the amorphous state of the annealed samples at all stages, as evidenced in Figure S5.

As shown in Figure 2b, multi-step rotating magnetic field annealing significantly improved the magnetic softness of the alloy, reducing the coercivity from 2.335 A/m in the as-cast state to 0.147 A/m and the remanence from 0.29 to 0.030 T. In contrast, although single-step annealing lowered the coercivity, it also increased the remanence, indicating only limited improvement in the overall magnetic softness.

As shown in Figure 2c, annealed samples exhibit a pronounced increase in permeability at low frequencies. The maximum and initial permeability values are summarized in Figure 2d. At low external field strengths,

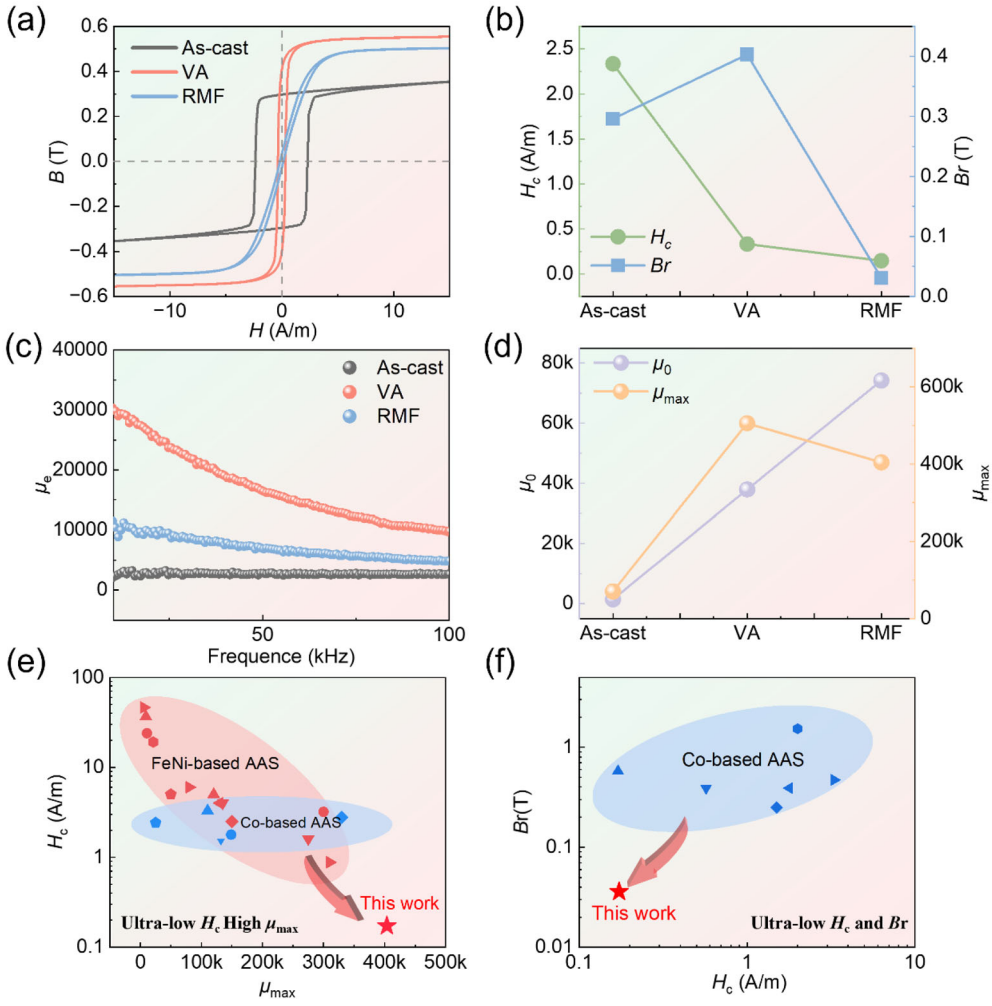

Figure 2. (a) M-H curves of core at different heat treatment stages. (b) Coercivity and remanence statistics of different heat treatment stages. (c) Effective permeability curves at different heat treatment stages. (d) Statistics on the initial permeability and maximum permeability at different heat treatment stages. (e) Performance statistics of coercivity and maximum permeability. (f) Performance statistics of remanence and coercivity.

shielding effectiveness depends primarily on the initial permeability — higher values correspond to better protection against weak magnetic fields. Under stronger fields, the operating point shifts toward the steepest portion of the magnetization curve, where maximum permeability governs the material's capacity to redirect magnetic flux. Thus, higher maximum permeability enables more efficient absorption and guidance of field lines, enhancing overall shielding performance. After annealing, the initial permeability of the as-cast samples increased from 1.4k to 74k, while the maximum permeability rose from 70k to 400k.

Figures 2e–f compared the coercivity, remanence, and maximum permeability of the RMF core with those of other FeNi and Co-based amorphous alloys [28–39]. The RMF core achieves an exceptional balance of properties, combining an ultra-low coercivity with an extraordinarily high maximum permeability (μ_{max} = 400k). This unique combination represents a significant advancement over existing amorphous alloys, offering both minimal magnetic hysteresis and superior magnetic flux guidance.

Figure 3a illustrates the magnetic shielding test, conducted entirely within a shielding barrel to eliminate interference from external fields. A Helmholtz coil inside the barrel generates a magnetic field controlled by a current source, with 1 mA corresponding to 132.005 nT. A magnetic field probe, enclosed in a cylindrical container wrapped with an RMF core and connected to an external monitoring device, is used to measure the field. The sample used for magnetic shielding testing is cylindrical, as shown in the enlarged section of Figure 3a. Its cylindrical surface and one end face are uniformly coated with a continuous layer of heat-treated ribbons. This layer has a consistent thickness of approximately 18 μm and exhibits no gaps between the individual ribbons. Prior to testing,

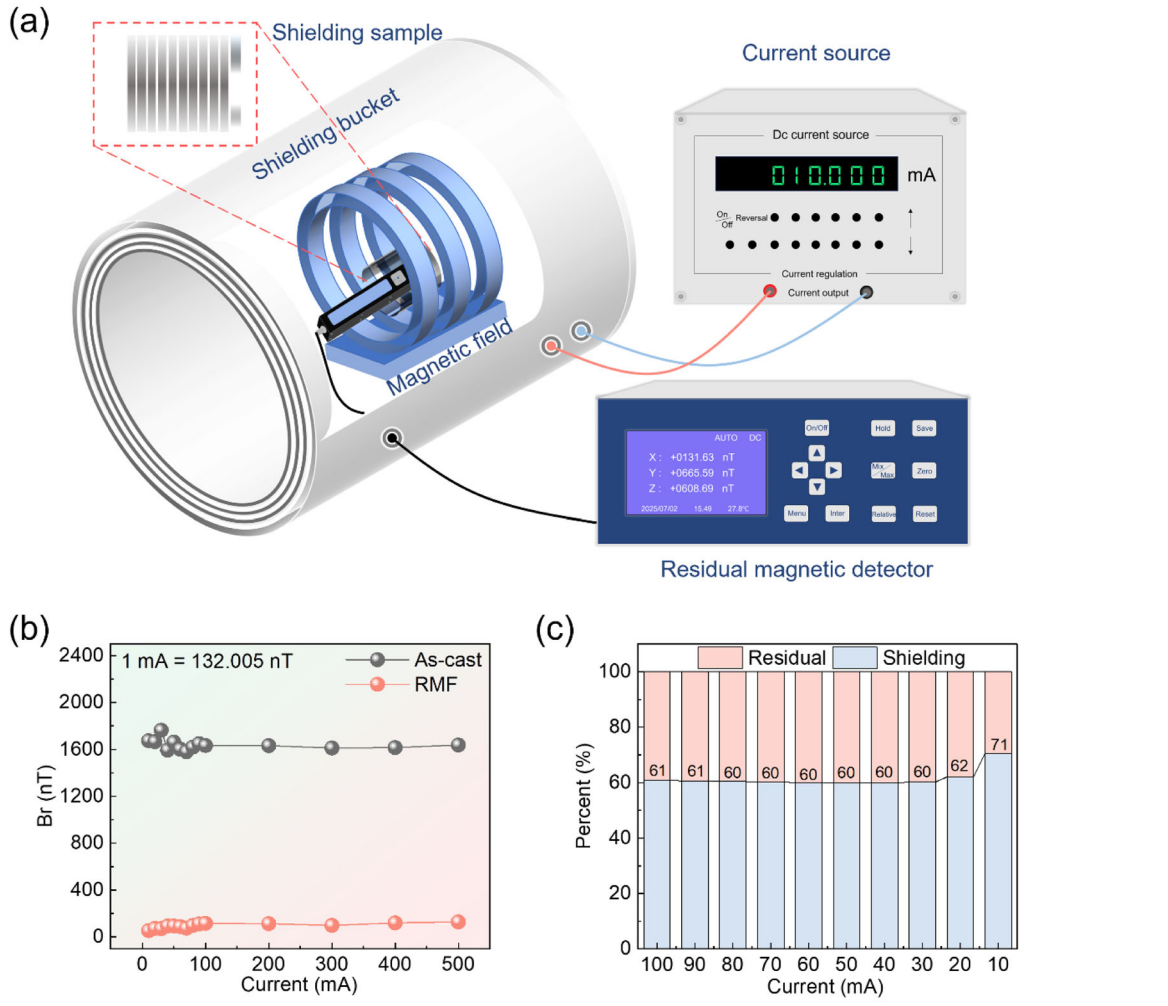

Figure 3. (a) Schematic diagram of residual magnetic field performance test. (b) Statistics on residual magnetic field inside after demagnetization. (c) Magnetic field shielding performance.

the probe is zero-calibrated. The material's shielding performance is then evaluated under varying magnetic field strengths, including measurements of residual fields after demagnetization.

Figure 3b shows the residual field strength as a function of applied current. As the current increases from 0 to 500 mA, cast and RMF samples exhibit distinct behaviors: the cast samples maintain high residual magnetic field (~1600 nT), while RMF samples stabilize near 80 nT. At low field levels, RMF samples perform even better, with residual magnetic field approaching 50 nT, whereas the cast samples show notable fluctuations. Figure 3c presents the dynamic-field shielding performance of RMF samples, with current increasing from 10 to 100 mA. In weak fields, the RMF samples achieve a shielding efficiency of up to 70%. As the field strength rises, the efficiency stabilizes around 60%. The performance of this magnetic shielding highlights the promising application potential of RMF samples, which combine high magnetic permeability with low residual magnetic field.

The atomic-scale topological order could also affect the magnetic properties of amorphous alloy. Figure 4b shows the reduced pair distribution function (PDF), G(r), for the As-cast and RMF sample, respectively, obtained by the fast Fourier transform of Q(S(Q)−1). The PDF reveals the structural information in real space, for typical regions of the As-cast sample and the deformed sample. An exponential decay function $f(r) = A \bullet \exp(-r/\xi)$ [40] was applied to estimate the decrease of peak height in the PDFs, which refers to the ordering degree [41]. A larger ξ value means a more correlated/ordered structure. The obtained ξ for the As-cast and RMF sample are 2.63 and 2.7 respectively, which may indicate that the ordering in RMF sample is more correlated than that of the As-cast sample.

The amorphous matrix is also influenced by magnetic field-assisted annealing. Figures 4c–e present TEM images of the as-cast and RMF cores. FFT analyses

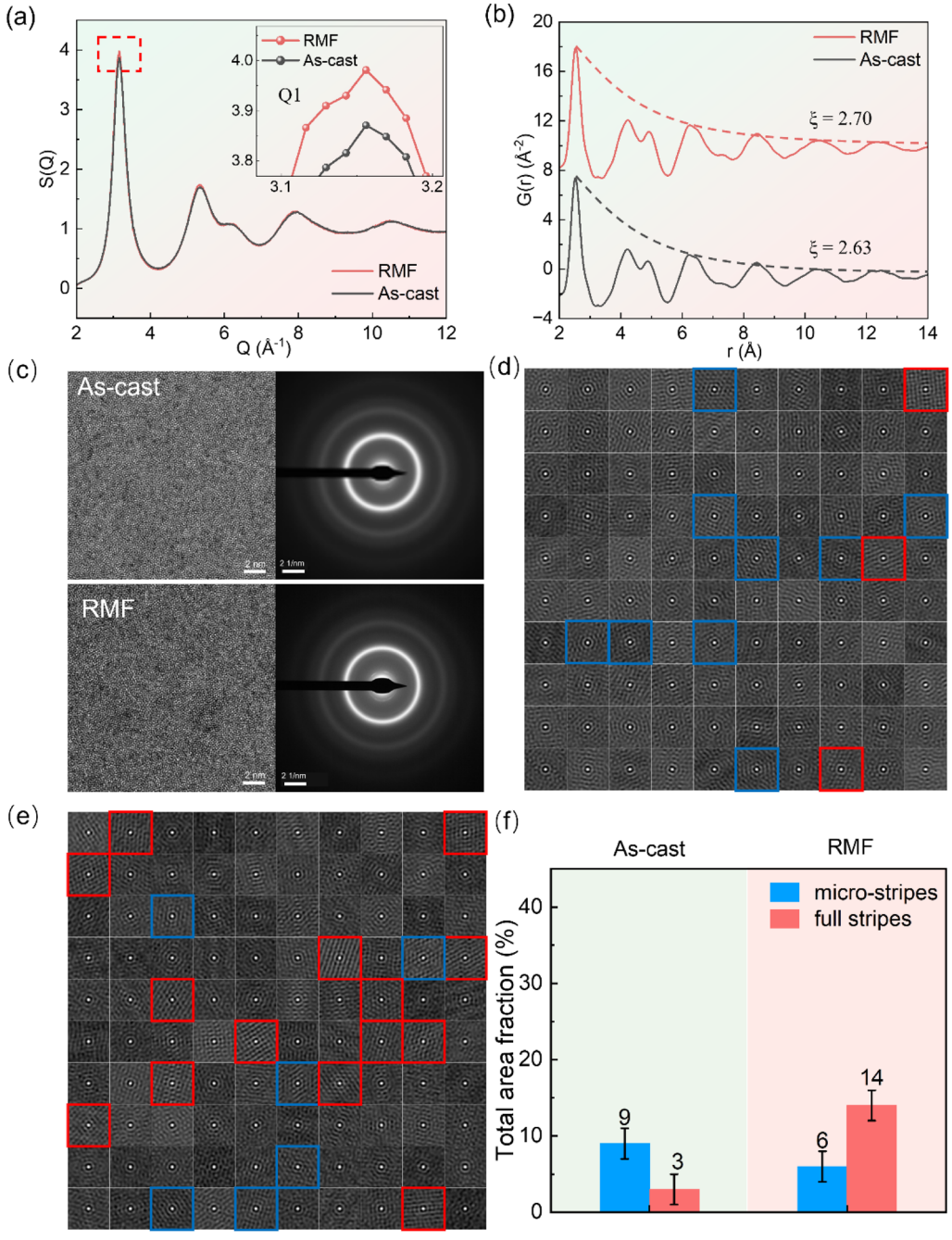

Figure 4. (a) The neutron and synchrotron structure factor S(Q) patterns of the As-cast and RMF sample. The inset shows the shift in position Q1 before and after the RMF. (b) The exponential function fitting of reduced PDF G(r) profiles for the cylinder sample before and after the RMF. The dotted lines are fitting results based on the exponential function. (c-e) Typical HRTEM images of the As-cast and RMF sample with the region highlighted by the red dashed square underwent FFT as the insets, and enlarged via auto-correlation analysis. (f) Total area fraction of MRO in the As-cast and RMF samples.

of regions in the amorphous matrix, indicated by red dashed squares, show ring patterns without spot features, confirming the amorphous state. These regions were enlarged and divided into 100 cells (1.80 × 1.80 nm⊃2), approximately corresponding to the size of medium-range order (MRO) [42,43]. Auto-correlation analysis using Digital Micrograph software revealed three distinct patterns: micro-stripes (highlighted in blue) and full stripes (highlighted in red), the remainder exhibits a fully amorphous structure. The corresponding uniform fast Fourier transform (FFT) image is shown in Figure S6. Micro-striped structures possess higher order than fully amorphous structures, while fully striped structures demonstrate the highest degree of order. Compares the average area percentage of crystal-like ordering between the As-cast and RMF cores shown in Figure 4f. Magnetic

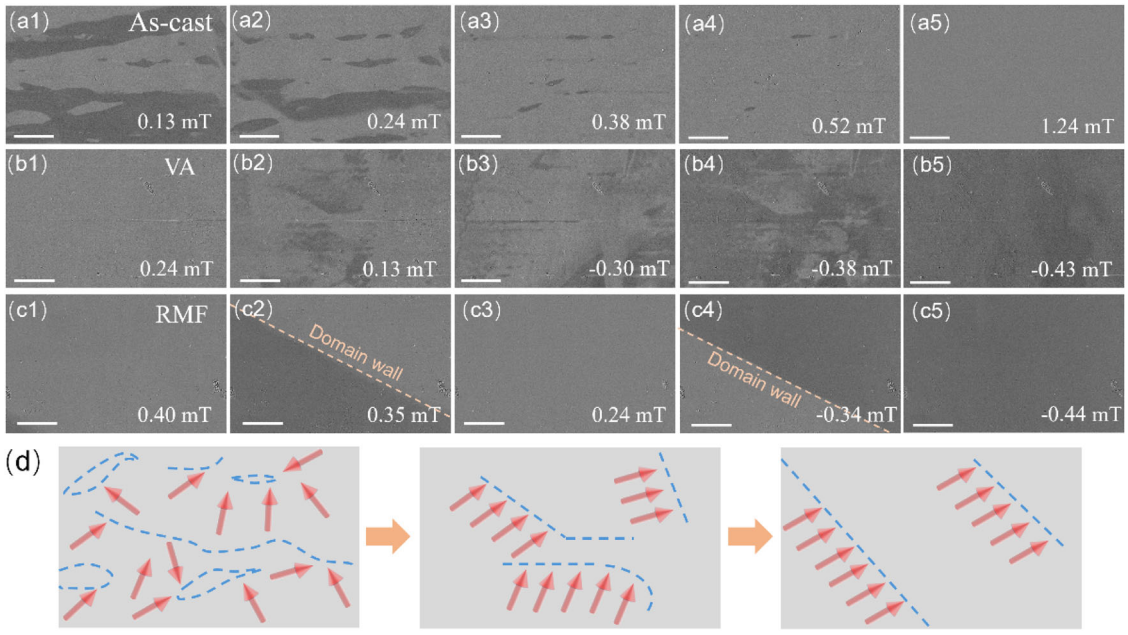

Figure 5. Evolution of the magnetic domain structures of the As-cast, VA and RMF. (a1–a5) Evolution of domain structure with different magnitudes of external magnetic fields of the As-cast sample using magneto-optical Kerr microscopy. (b1–b5) Evolution of domain structure with different magnitudes of external magnetic fields of the VA sample using magneto-optical Kerr microscopy. (c1–c5) Evolution of domain structure with different magnitudes of external magnetic fields of the RMF sample using magneto-optical Kerr microscopy. (d) The schematic drawing of the domain wall movement mechanism on the surface of alloy samples from front view.

field-assisted annealing increases the fraction of MRO, with the RMF core exhibiting the highest percentage (20%) compared to the As-cast core (12%).

After optimal heat treatment, internal stresses are completely relieved. With the increase in MRO, the RMF sample exhibits highly flexible magnetization vectors under such low effective anisotropy, showing little tendency to lock into a specific orientation. Once the external field is removed, domain walls move freely, allowing the magnetization vectors to rapidly relax to the lowest-energy configuration — the demagnetized state [44–47], where the magnetization vectors of individual domains cancel each other — resulting in extremely low remanence.

In contrast, although the As-cast material with low structural order does not exhibit pronounced magneto crystal line anisotropy, it contains significant internal stresses and compositional heterogeneities. These factors induce magnetoelastic anisotropy, which creates pinning sites for magnetic domain walls. Upon removal of an external magnetic field, these pinning sites hinder the full restoration of magnetic domains to the demagnetized state [47]. As a result, a fraction of the magnetization vectors remains 'frozen' along the direction of the previously applied field, leading to a higher remanent magnetization.

With the enhancement of medium-range order (MRO), a more correlated and structurally relaxed amorphous matrix reduces local structural heterogeneity, suppresses effective magnetic anisotropy and magnetoelastic anisotropy, and decreases the density of pinning sites for domain-wall motion. As a result, domain walls can move more freely under an external field, leading to higher permeability and lower coercivity. At the same time, once the field is removed, the magnetization can more readily return to a low-energy demagnetized configuration, which explains the greatly reduced remanence.

In addition to static magnetic domain structures, the RMF core exhibits a distinct dynamic response under alternating magnetic fields, which plays a decisive role in its low-frequency soft magnetic performance. Figure 5 presents Kerr images showing the dynamic evolution of domain structures in As-cast, VA and RMF samples with the magnetic field applied parallel to the ribbon axis. The domain-wall motion mechanisms differ markedly between the three samples (As-cast, VA and RMF), resulting in significant differences in low-frequency permeability and remanence.

As shown in Figure 5, magnetic domains undergo significant changes during annealing. In the As-cast sample, the domains appear fragmented. Vacuum annealing reduces this fragmentation, although some pinning effects remain. Only after RMF annealing do the

domain walls form large, well-defined regions with regular, orderly shapes. The schematic diagram in Figure 5d more clearly illustrates the evolution of magnetic domains. Starting from randomly oriented fragmented domains, they gradually develop a certain degree of alignment. With increasing annealing, they ultimately transform into large, uniformly oriented domains.

High magnetic permeability and low remanence are two sides of the same coin, both reflecting the ease with which magnetization vectors rotate within a material. Microscopically, this corresponds to a highly 'soft' and responsive magnetic domain structure, where defects that could pin domain walls are virtually absent [48–50]. As a result, domain walls move almost frictionlessly, allowing substantial reversible displacement under minimal changes in the applied magnetic field — this is the core reason for high permeability. Simultaneously, when the external field is removed, this near-frictionless mobility prevents magnetization vectors from remaining 'frozen' in their prior orientations. Driven by demagnetization energy, they rapidly rearrange into low-energy closed-flux configurations, causing the magnetization within each domain to largely cancel out. Therefore, high permeability and low remanence originate from the same microscopic mechanism: extremely low effective magnetic anisotropy and highly free domain wall motion. Thus, the RMF samples demonstrate excellent magnetic properties, combining high permeability with low remanence.

3. Conclusion

In summary, this work presents an effective material-processing strategy that overcomes a long-standing challenge in low-frequency magnetic shielding. By multi-applying a multi-step rotating magnetic field (MS-RMF) annealing process to a Co-based amorphous alloy, we simultaneously achieve an ultra-low residual magnetic field (~ 50 nT) and ultra-high permeability (~ 400000), along with an extremely low coercivity of 0.147 A/m. These properties collectively enable a magnetic shielding effectiveness of up to 70% in the sub-100 kHz regime. The exceptional performance is attributed to the MS-RMF-induced formation of a structurally relaxed and ordered atomic arrangement, which strongly suppresses effective magnetic anisotropy and thus facilitates nearly free domain-wall motion and rapid magnetization response. This study establishes a powerful material-design and processing route for next-generation soft-magnetic materials, offering a promising solution for high-sensitivity, low-frequency electromagnetic protection.

Author contributions

CRediT: **Yuyang Qian:** Conceptualization, Data curation, Investigation, Methodology, Resources, Validation, Writing – original draft; **Chaoqun Pei:** Formal analysis, Supervision, Validation; **Congrui Yang:** Formal analysis, Supervision, Validation; **Zida Zhang:** Supervision, Validation, Visualization; **Zhichao Lu:** Formal analysis, Supervision, Validation; **Dong Ma:** Investigation, Validation, Visualization; **Ke Yang:** Investigation, Methodology, Visualization; **Jiang Ma:** Validation, Visualization; **Baoan Sun:** Funding acquisition, Writing – review & editing; **Haibo Ke:** Funding acquisition, Project administration, Writing – review & editing; **Gang Wang:** Funding acquisition, Visualization, Writing – review & editing; **Weihua Wang:** Validation, Visualization.

Disclosure statement

No potential conflict of interest was reported by the authors.

Funding

This work was financially supported by National Natural Science Foundation of China (No. 52571192, 52192602, 52192601, U23A2065), the Guangdong Basic and Applied Basic Research, China (Grant No. 2024B1515120012), the Guangdong Province Key Research and Development Program (2026B0101040002), Guangdong Talent Program (Grant No. 2024TQ08C641), Guangdong Provincial Quantum Science Strategic Initiative (GDZX2402001), the AI-driven experiments, simulations, and model training were performed on the robotic AI-Scientist platform of Chinese Academy of Sciences. The National Key R&D Program of China (No. 2024YFB3411500), the Innovation Program of Shanghai Municipal Education Commission (No.2021-01-07-00-09-E00114), the Technology Plan Program of Shanghai Municipal Commission of Science and Technology (No. 25CL2902300) and the Shanghai Municipal Explorer Program (No. 25TS1401900), the open research fund of Songshan Lake Materials Laboratory (2023SLABFN07). We thank the Shanghai Synchrotron Radiation Facility of BL12SW (https://cstr.cn/31124.02.SSRFBL12SW) for the assistance on HE-XRD measurements (the SSRF proposal No. 2024-SSRF-PT-508929).

References

[1] Prekodravac Filipovic J, Milenkovic M, Kepic D, et al. Electromagnetic interference in the modern era: concerns, trends, and nanomaterial-based solutions. Nanomaterials. 2025;15(20):1558.
[2] Jia X, Li Y, Shen B, et al. Evaluation, fabrication and dynamic performance regulation of green EMI-shielding materials with low reflectivity: a review. Compos B Eng. 2022;233:109652.
[3] Lu Z, Jia F, Zhuo L, et al. Micro-porous MXene/Aramid nanofibers hybrid aerogel with reversible compression and efficient EMI shielding performance. Compos B Eng. 2021;217:108853.
[4] Chen Y, Zhang HB, Yang Y, et al. High-performance epoxy nanocomposites reinforced with three-dimensional carbon

nanotube sponge for electromagnetic interference shielding. Adv Funct Mater. 2016;26(3):447–455.
[5] Song Q, Ye F, Yin X, et al. Carbon nanotube–multilayered graphene edge plane core–shell hybrid foams for ultrahigh-performance electromagnetic-interference shielding. Adv Mater. 2017;29(31):1701583.
[6] Iqbal A, Shahzad F, Hantanasirisakul K, et al. Anomalous absorption of electromagnetic waves by 2D transition metal carbonitride Ti3CNTx (MXene). Science. 2020;369(6502):446–450.
[7] Wang Z, Mao B, Wang Q, et al. Ultrahigh conductive copper/large flake size graphene heterostructure thin-film with remarkable electromagnetic interference shielding effectiveness. Small. 2018;14(20):1704332.
[8] Hayashi Y-i. State-of-the-art research on electromagnetic information security. Radio Sci. 2016;51(7):1213–1219.
[9] Jie H, Zhao Z, Zeng Y, et al. A review of intentional electromagnetic interference in power electronics: Conducted and radiated susceptibility. IET Power Electron. 2024;17(12):1487–1506.
[10] Xu X, Liu W, Huang Y, et al. Magnetic shielding mechanism and structure design of composites at low frequency: a review. J Magn Magn Mater. 2023;570:170509.
[11] Liu Y, Yang J, Cao F, et al. Enhancement of magnetic shielding based on low-noise materials, magnetization control, and active compensation: a review. Materials (Basel). 2024;17(22):5469.
[12] Shahzad F, Alhabeb M, Hatter CB, et al. Electromagnetic interference shielding with 2D transition metal carbides (MXenes). Science. 2016;353(6304):1137–1140.
[13] Sun J, Ji A, Wang P, et al. Nyquist magnetic noise analysis and experiments of low-frequency shielding soft magnetic materials. Sens Actuators, A. 2025;382:116113.
[14] Yang Y, Oyedeji TD, Zhou X, et al. Tailoring magnetic hysteresis of additive manufactured Fe-Ni permalloy via multiphysics-multiscale simulations of process-property relationships. Npj Comput Mater. 2023;9(1):103.
[15] Sun J, Ren J, Li J, et al. Measurement and analysis of magnetic properties of permalloy for magnetic shielding devices under different temperature environments. Materials (Basel). 2023;16(8):3253.
[16] Yang J, Shi M, Zhang X, et al. Demagnetization parameters evaluation of magnetic shields based on anhysteretic magnetization curve. Materials (Basel). 2023;16(15):5238.
[17] Voigt J, Knappe-Grüneberg S, Schnabel A, et al. Measures to reduce the residual field and field gradient inside a magnetically shielded room by a factor of more than 10. Metrol Meas Syste. 2013;20(2):8229.
[18] Cheng Y, Luo Y, Shen R, et al. Testing and analysis method of low remanence materials for magnetic shielding device. Materials (Basel). 2023;16(2):681.
[19] Thiel F, Schnabel A, Knappe-Grüneberg S, et al. Demagnetization of magnetically shielded rooms. Rev Sci Instrum. 2007;78(3):5106.
[20] Wang Z, Li H, Yang S, et al. Modeling and experimental studies of degaussing hysteresis in near-zero magnetic shielding systems. J Appl Phys. 2024;135(8):4501.
[21] Murali P, Ramamurty U. Embrittlement of a bulk metallic glass due to sub-Tg annealing. Acta Mater. 2005;53(5):1467–1478.
[22] Huang X, Ramirez A. Structural relaxation and crystallization of NiTi thin film metallic glasses. Appl Phys Lett. 2009;95(12):1911.
[23] Launey M, Busch R, Kruzic J. Effects of free volume changes and residual stresses on the fatigue and fracture behavior of a Zr–Ti–Ni–Cu–Be bulk metallic glass. Acta Mater. 2008;56(3):500–510.
[24] Pei C, Chen S, Zhao T, et al. Nanostructured metallic glass in a highly upgraded energy state contributing to efficient catalytic performance. Adv Mater. 2022;34(26):2200850.
[25] Zhang BH, Liu JH, Zhou HT. Comprehensive study of the crystallization behavior, thermal stability, and magnetic properties of Co66. 5Si15. 5B12Fe4Ni2 amorphous ribbon. J Non-Cryst Solids. 2021;573:121132.
[26] Yoon S, Kwon S, Kim J-H, et al. Determination of magnetization rotation and domain wall motion components in reversible complex susceptibility spectra of Co-based amorphous ribbons with various annealing times. J Magn Magn Mater. 2002;242:261–264.
[27] Mallick S, Sharma P, Takenaka K, et al. Static and dynamic behavior of domain walls in high BS soft magnetic ribbons tuned by the annealing temperature. J Phys D: Appl Phys. 2018;51(6):065007.
[28] Spilka M, Griner S, Kania A. Properties changes of Co-based amorphous alloy in thermal activation process. Arch Mater Sci Eng. 2013;64(2):118–124.
[29] Kachniarz M. The magnetoelastic properties of Co-based amorphous alloy under torque operation. Acta Phys Pol A. 2024;146(4):558–562.
[30] Konieczny J, Borisjuk A, Pashechko M, et al. Magnetic properties of Co-based amorphous ribbon under cyclic heating and cooling. Structure. 2010;25:26.
[31] Castro R, Prasad S, Gomes R, et al. Preparation and characterization of Co 80 Nb 20-x B x amorphous metallic ribbons. J Therm Anal Calorim. 2004;75(2):649–654.
[32] Su M, Zhuang Y, Pan L, et al. Optimizing Cr-doped Co-based amorphous alloys for high-performance fluxgate current sensors. J Alloys Compd. 2025;1030:180905.
[33] Liren Z, Xin Y, Yang P, et al. Magnetic performance measurement and mathematical model establishment of main core of magnetic modulator. 2017 13th IEEE International Conference on Electronic Measurement & Instruments (ICEMI); 2017: IEEE.
[34] Gavrila H, Ionita V. Crystalline and amorphous soft magnetic materials and their applications- status of art and challenges. J Optoelectron Adv Mater(Romania). 2002;4(2):173–192.
[35] Quach HP, Chui TCP. Low temperature magnetic properties of Metglas 2714A and its potential use as core material for EMI filters. Cryogenics. 2004;44(6-8):445–449.
[36] Azuma D, Hasegawa R. Core loss in toroidal cores based on Fe-based amorphous Metglas 2605HB1 alloy. IEEE Trans Magn. 2011;47(10):3460–3462.
[37] Byerly K, Krimer Y, Phatak C, et al. Magnetostrictive loss reduction through stress relief annealing in an FeNi-based metal amorphous nanocomposite. J Mater Res. 2021;36(14):2843–2855.
[38] Kiran MR, Islam MR, Muttaqi KM, et al. Characterization of amorphous soft magnetic materials for toroidal core multi-winding medium frequency transformers. 2017

IEEE Region 10 Humanitarian Technology Conference (R10-HTC); 2017: IEEE.
[39] Tsepelev V, Starodubtsev YN, Tsepeleva N. Hysteresis properties of the amorphous high permeability Co66Fe3Cr3Si15B13 alloy. AIP Adv. 2018;8(4):7707.
[40] Ma D, Stoica AD, Wang X-L. Power-law scaling and fractal nature of medium-range order in metallic glasses. Nat Mater. 2009;8(1):30–34.
[41] Lan S, Wu Z, Wei X, et al. Structure origin of a transition of classic-to-avalanche nucleation in Zr-Cu-Al bulk metallic glasses. Acta Mater. 2018;149:108–118.
[42] Elliott SR. Medium-range structural order in covalent amorphous solids. Nature. 1991;354(6353):445–452.
[43] Ma D, Stoica AD, Yang L, et al. Nearest-neighbor coordination and chemical ordering in multicomponent bulk metallic glasses. Appl Phys Lett. 2007;90(21):1908.
[44] He N, Song L, Xu W, et al. The evolution of relaxation modes during isothermal annealing and its influence on properties of Fe-based metallic glass. J Non-Cryst Solids. 2019;509:95–98.
[45] Im S, Wang Y, Zhao P, et al. Medium-range ordering, structural heterogeneity, and their influence on properties of Zr-Cu-Co-Al metallic glasses. Phys Rev Mater. 2021;5(11):115604.
[46] Ito N, Suzuki K. Improvement of magnetic softness in nanocrystalline soft magnetic materials by rotating magnetic field annealing. J Appl Phys. 2005;97(10):503.
[47] Olivera J, Varga R, Prida V, et al. Domain wall dynamics during the devitrification of Fe 73.5 CuNb 3 Si 11.5 B 11 magnetic microwires. Phys Rev B—Conden Matter Mater Phys. 2010;82(9):094414.
[48] Silveyra JM, Ferrara E, Huber DL, et al. Soft magnetic materials for a sustainable and electrified world. Science. 2018;362(6413):eaao0195.
[49] Casiraghi A, Dominguez TR, Rößler S, et al. Influence of elastically pinned magnetic domain walls on magnetization reversal in multiferroic heterostructures. Phys Rev B. 2015;92(5):4406.
[50] Cai M, Wang J, Wang Q, et al. Improvement of soft-magnetic properties for Fe-based amorphous alloys with high saturation polarization by stress annealing. Mater Res Lett. 2023;11(7):595–603.